

Three-dimensional printing of transparent fused silica glass

Frederik Kotz¹, Karl Arnold¹, Werner Bauer², Dieter Schild³, Nico Keller¹, Kai Sachsenheimer¹, Tobias M. Nargang¹, Christiane Richter¹, Dorothea Helmer¹ & Bastian E. Rapp¹

Glass is one of the most important high-performance materials used for scientific research, in industry and in society, mainly owing to its unmatched optical transparency, outstanding mechanical, chemical and thermal resistance as well as its thermal and electrical insulating properties^{1–3}. However, glasses and especially high-purity glasses such as fused silica glass are notoriously difficult to shape, requiring high-temperature melting and casting processes for macroscopic objects or hazardous chemicals for microscopic features^{3,4}. These drawbacks have made glasses inaccessible to modern manufacturing technologies such as three-dimensional printing (3D printing). Using a casting nanocomposite⁵, here we create transparent fused silica glass components using stereolithography 3D printers at resolutions of a few tens of micrometres. The process uses a photocurable silica nanocomposite that is 3D printed and converted to high-quality fused silica glass via heat treatment. The printed fused silica glass is non-porous, with the optical transparency of commercial fused silica glass, and has a smooth surface with a roughness of a few nanometres. By doping with metal salts, coloured glasses can be created. This work widens the choice of materials for 3D printing, enabling the creation of arbitrary macro- and microstructures in fused silica glass for many applications in both industry and academia.

Until now, only two ways to shape glass in a 3D printing process have been demonstrated: a fused deposition moulding approach in which soda lime glass is heated to around 1,000 °C and a manual wire feeding approach in which a glass filament is melted using a laser beam^{6–8}. In both cases, coarse structures with high surface roughness are obtained. Approaches such as inkjet printing, selective laser melting or sintering of glass powders have so far led only to white non-transparent glass components^{9–12}. Stop-flow lithography has been used to shape glass directly but was limited to two-dimensional fused silica microstructures¹³. Three-dimensional direct laser writing has

been used to shape fused silica surfaces by damaging the irradiated area and dissolving the damaged area in a subsequent hydrofluoric acid (HF) etching step. However, the resulting structures are too rough for optical applications, for example, and require further post-processing such as CO₂-laser annealing¹⁴.

Here we describe a 3D-printing-compatible approach to manufacturing high-quality fused silica glass components using stereolithography, microlithography and microstereolithography. This process circumvents the size and resolution limits associated with state-of-the-art methods for glass structuring. It does not require harsh chemicals and produces surfaces of optical clarity and reflectivity suitable for the design of optical components such as lenses and filters.

Amorphous silica nanoparticles with a mean diameter of 40 nm were dispersed in a monomeric matrix. The monomeric matrix mainly consists of the monomer hydroxyethylmethacrylate (HEMA), which allows the dispersion of high amounts of silica nanoparticles owing to the formation of a solvation layer, without using further additives¹⁵. The nanocomposite was then shaped with stereolithography using free radical polymerization, resulting in the so-called ‘green part’. The resulting green part can be further polymerized thermally or by an additional floodlight-exposure step. Non-polymerized material is removed during development by immersion in a solvent. The green part was then thermally debound—that is, the polymeric matrix (binder) was removed by heating which results in thermal decomposition—resulting in the so-called ‘brown part’ (see Extended Data Fig. 1a). During a final sintering step at 1,300 °C the density of the brown part is increased ($\rho_{\text{final}} = 2.2 \text{ g cm}^{-3}$) to that of high-quality fused silica glass with no remaining porosity and no cracks. The whole process is shown in Fig. 1a. The programme for the heat treatment can be seen in Extended Data Fig. 1b. The resulting glass consists of pure fused silica glass as ascertained by X-ray photoelectron spectroscopy (see Fig. 2a and Extended Data Fig. 2a). Raman spectroscopy and X-ray diffraction

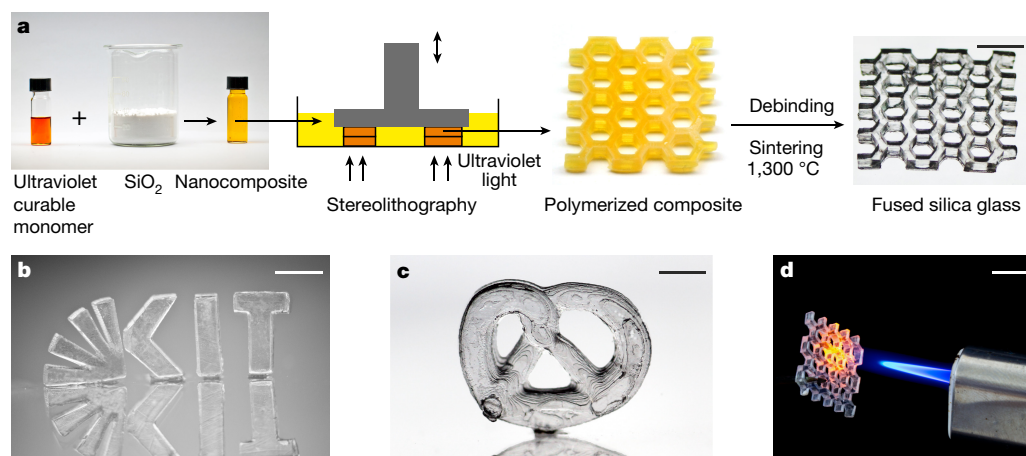


Figure 1 | 3D printing of fused silica glass. **a**, Ultraviolet-curable monomer mixed with amorphous silica nanopowder is structured in a stereolithography system. The resulting polymerized composite is turned into fused silica glass through thermal debinding and sintering (scale bar, 7 mm). **b**, **c**, Examples of printed and sintered glass structures: Karlsruhe Institute of Technology logo (**b**; scale bar, 5 mm) and pretzel (**c**; scale bar, 5 mm). **d**, Demonstration of the high thermal resistance of printed fused silica glass (scale bar, 1 cm). The flame had a temperature of about 800 °C.

¹Institute of Microstructure Technology (IMT), Karlsruhe Institute of Technology (KIT), Hermann-von-Helmholtz-Platz 1, Eggenstein-Leopoldshafen 76344, Germany. ²Institute for Applied Materials (IAM), KIT, Hermann-von-Helmholtz-Platz 1, Eggenstein-Leopoldshafen 76344, Germany. ³Institute for Nuclear Waste Disposal (INE), KIT, Hermann-von-Helmholtz-Platz 1, Eggenstein-Leopoldshafen 76344, Germany.

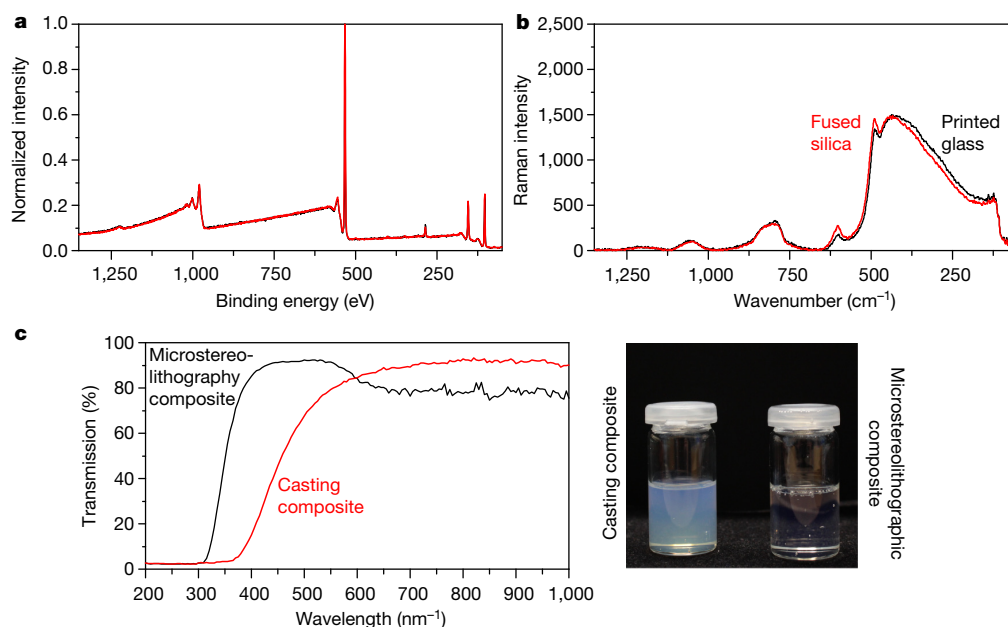


Figure 2 | Characterization of sintered glass and high resolution nanocomposite. **a**, **b**, X-ray photoelectron spectroscopy (**a**) and Raman spectrum (**b**) of printed and sintered glass compared to commercial fused silica glass. **c**, Left, ultraviolet-visible transmission of the index-matched nanocomposite for microstereolithography and the non-index-matched casting slurry⁵. At 365 nm (i-line) the transmission of the microstereolithography nanocomposite is increased by about 62%. The microstereolithography nanocomposite is highly transparent (about 66% transmission) while the casting slurry is strongly absorbing (about 4% transmission). Right, the casting and the microstereolithography nanocomposites.

were performed to demonstrate that no devitrification occurs during the sintering process and the resulting glass is fully amorphous (see Fig. 2b and Extended Data Fig. 2b).

The basis for this work is a nanocomposite that we developed for bulk polymerization⁵. This nanocomposite can be cured by light but does not allow high-resolution photostructuring. High-resolution microstereolithography is only possible for nanocomposites with an optimal index-matched monomer/particle system to minimize scattering effects and a low viscosity combined with high amounts of crosslinking agents to achieve a high contrast¹⁶. By removing the solvent we reduced the viscosity of the nanocomposite and achieved a better index match between the particles and the monomer mixture. As can be seen in Fig. 2c, the index-matched microstereolithography nanocomposite shows an optical transmission of approximately 66% at a wavelength of 365 nm (i-line; the processing wavelength), whereas the blurry casting nanocomposite has a transparency of only roughly 4%. High transmission of the nanocomposite at the processing wavelength is a requirement for high-resolution (stereo)lithography. We further increased the degree of chemical crosslinking by using higher-molecular-weight triacrylates and changed the initiator system to achieve an appropriate cure speed as well as mechanical and chemical stability for high-contrast development. An absorber and an inhibitor were added to increase the lateral resolution and to control *z*-overcuring (where *x*–*y* is the building plane, and *z* is in the printing direction facing upwards) errors. The nanocomposites are highly stable and can be stored in the refrigerator for weeks without any sedimentation effects or change in printing parameters (see Extended Data Fig. 1c).

The nanocomposites can be processed in cost-effective benchtop stereolithography printers (Asiga Pico 2), allowing for the creation of fully three-dimensional glass components in a layer-by-layer fashion. Figure 1 shows exemplary glass components made by this process displaying high printing accuracy. The printed and sintered fused silica glass parts possess extremely low thermal expansion coefficients of $\alpha_{20-600} = 0.52 \times 10^{-6} \text{ K}^{-1}$, which is the same value as for commercial fused silica. This leads to very high thermal shock resistance of the material (see Fig. 1d)¹⁷.

Printing the nanocomposites yields glass feature resolutions and structure quality fully compatible with the demands of microelectromechanical systems (MEMS), microoptical and microfluidic applications, as can be seen in Fig. 3. A custom-built micro(stereo-)lithography system based on a digital mirror device was used to shape fused silica glass at a resolution of a few tens of micrometres, having sharp edges that cannot be achieved with classical glass-structuring techniques¹⁸. Figure 3a shows an exemplary hollow castle gate in fused silica glass which was fabricated using microstereolithography (the pinnacles on top of the turrets have a diameter of 80 μm). The nanocomposites can also be used as a negative photoresist for microlithography. Figure 3b shows a microfluidic glass chip—a Tesla mixer cascade—which was structured using microlithography. The micro-optical diffractive element shown in Fig. 3c was structured and sintered on top of a commercial fused silica slide. Gradients in the exposure dose can be used to generate surface reliefs via greyscale lithography, such as the array of glass microlenses shown in Fig. 3d. As expected for fused silica glass, none of these microstructured glass parts showed any swelling, defects

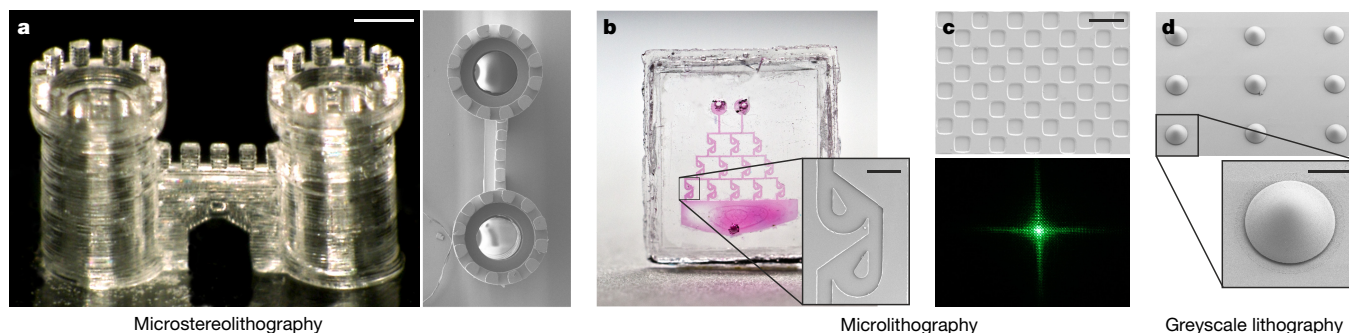


Figure 3 | Microstructuring of fused silica glass. **a**, Microstereolithography of a hollow castle gate (scale bar, 270 μm). **b**, Microlithography of an exemplary microfluidic chip (inset scale bar, 200 μm). **c**, Micro-optical

diffractive structure creating the optical projection pattern shown at the bottom (illuminated with a green laser pointer; scale bar, 100 μm). **d**, Microlenses fabricated using greyscale lithography (inset scale bar, 100 μm).

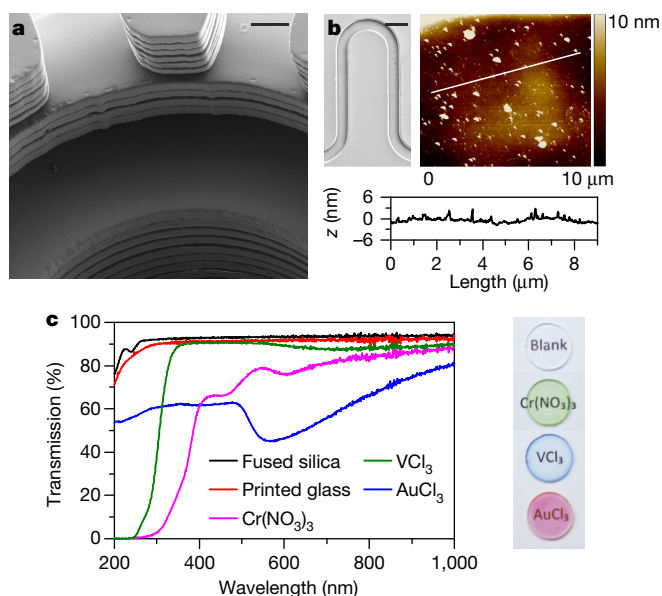


Figure 4 | Surface and optical characterization of sintered glass. **a**, The printed glass part shows the steps and side wall undulations from the layer-by-layer microstereolithography process. The part was printed with a 20-μm layer thickness (scale bar, 80 μm). **b**, Atomic force microscope measurement on a microfluidic channel in fused silica glass, showing very low surface roughness of the top surfaces of about 2 nm (scale bar, 260 μm); *z* is the measured height of the sample. **c**, Ultraviolet–visible transmission of printed and sintered glass compared to commercial fused silica. The transmission spectra are almost identical. Doping of sintered glass with metal salts leads to coloured binary fused silica glasses (shown on the right).

or optical alteration when exposed to hazardous chemicals (acids, bases, alcohols, ketones, haloalkanes, aromatic and aliphatic hydrocarbons). The shrinkage of the part during the sintering process is isotropic and dependent on the solid loading (hence can be calculated; see Supplementary Information). The sintering shrinkage for stereolithography and microstereolithography does not depend on the scale of the sintered parts (for example, the honeywell structure in Fig. 1a with a solid loading of 37.5 vol% showed the expected linear shrinkage of 27.88% in height from 3.05 mm to 2.2 mm and width from 2.177 cm to 1.57 cm).

The structures are translated with high fidelity from the green part to the glass components. Even the undulations caused by the stereolithography process such as the typical steps at the side walls from the layer-by-layer printing process can be seen in the final glass part (see Fig. 4a). On the other hand, glass components made via microlithography as well as the top surfaces of stereolithography printed parts show exceptionally smooth surfaces with a roughness of about 2 nm, suitable for optical applications (see Fig. 4b). These smooth sintered glass components show the same transparency in the ultraviolet, visible and infrared parts of the spectrum as commercial fused silica glass (see Fig. 4c and Extended Data Fig. 2c).

The workflow allows for modifications of the optical properties of the glass components in the brown part state by doping with alcoholic metal salt solutions, thereby creating coloured glasses suitable, for example, for optical filters¹⁹. Chromium(III) nitrate (Cr(NO₃)₃) resulted in a green-coloured glass and vanadium(III) chloride (VCl₃) resulted in a blue-coloured glass. Doping with gold(III) chloride (AuCl₃) resulted in the formation of gold nanoparticles inside the glass, producing colloidal red colouring (see Fig. 4c)^{20,21}.

In summary, we describe a 3D-printing-compatible process for creating high-quality transparent fused silica glass components. 3D printing of fused silica glass will enable the construction of complex shapes of highly transparent, temperature- and chemical-resistant glass on the macro- and microscale. This process makes one of the

oldest materials known to mankind accessible to modern 3D printing techniques.

Online Content Methods, along with any additional Extended Data display items and Source Data, are available in the online version of the paper; references unique to these sections appear only in the online paper.

Received 8 December 2016; accepted 7 March 2017.

- Hench, L. L., Day, D. E., Höland, W. & Rheinberger, V. M. Glass and medicine. *Int. J. Appl. Glass Sci.* **1**, 104–117 (2010).
- Ikushima, A., Fujiwara, T. & Saito, K. Silica glass: a material for photonics. *J. Appl. Phys.* **88**, 1201–1213 (2000).
- Bansal, N. P. & Doremus, R. H. *Handbook of Glass Properties* 680 (Elsevier, 2013).
- Hülsmberg, D., Harnisch, A. & Bismarck, A. *Microstructuring of Glasses* 1st edn, Vol. 87, 323 (Springer, 2005).
- Kotz, F. et al. Liquid glass: a facile soft replication method for structuring glass. *Adv. Mater.* **28**, 4646–4650 (2016).
- Klein, J. et al. Additive manufacturing of optically transparent glass. *3D Print. Additive Manuf.* **2**, 92–105 (2015).
- Luo, J. et al. in *Proc. Conf. SPIE LASE 97380Y–97380Y-9*, <http://dx.doi.org/10.1117/12.2218137> (International Society for Optics and Photonics, 2016).
- Luo, J., Pan, H. & Kinzel, E. C. Additive manufacturing of glass. *J. Manuf. Sci. Eng.* **136**, 061024 (2014).
- Klein, S., Simske S., Parraman C., Walters P., Huson D. & Hoskins S. *3D Printing of Transparent Glass* Technical Report HPL-2012-198, <http://www.hpl.hp.com/techreports/2012/HPL-2012-198.pdf> (Hewlett Packard Labs, 2012).
- Marchelli, G., Prabhakar, R., Storti, D. & Ganter, M. The guide to glass 3D printing: developments, methods, diagnostics and results. *Rapid Prototyping J.* **17**, 187–194 (2011).
- Fateri, M. & Gebhardt, A. Selective laser melting of soda-lime glass powder. *Int. J. Appl. Ceram. Technol.* **12**, 53–61 (2015).
- Klocke, F., McClung, A. & Ader, C. in *Proc. Solid Freeform Fabrication Symp.* 214–219, <https://sffsymposium.engr.utexas.edu/Manuscripts/2004/2004-21-Klocke.pdf> (2004).
- Shepherd, R. F. et al. Stop-flow lithography of colloidal, glass, and silicon microcomponents. *Adv. Mater.* **20**, 4734–4739 (2008).
- Lin, J. et al. On-chip three-dimensional high-Q microcavities fabricated by femtosecond laser direct writing. *Opt. Express* **20**, 10212–10217 (2012).
- Raghavan, S. R., Walls, H. & Khan, S. A. Rheology of silica dispersions in organic liquids: new evidence for solvation forces dictated by hydrogen bonding. *Langmuir* **16**, 7920–7930 (2000).
- Sun, C. & Zhang, X. The influences of the material properties on ceramic micro-stereolithography. *Sens. Actuators A* **101**, 364–370 (2002).
- Souder, W. H. & Hidnert, P. *Measurements on the Thermal Expansion of Fused Silica 3* (Government Printing Office, 1926).
- Waldbaur, A., Carneiro, B., Hettich, P., Wilhelm, E. & Rapp, B. Computer-aided microfluidics (CAMF): from digital 3D-CAD models to physical structures within a day. *Microfluid. Nanofluid.* **15**, 625–635 (2013).
- Clasen, R. Preparation of coloured silica glasses made by sintering of particulate gels. *Glastechnische Berichte* **66**, 299–304 (1993).
- Schultz, P. C. Optical absorption of the transition elements in vitreous silica. *J. Am. Ceram. Soc.* **57**, 309–313 (1974).
- Kozuka, H. & Sakka, S. Preparation of gold colloid-dispersed silica-coating films by the sol-gel method. *Chem. Mater.* **5**, 222–228 (1993).

Supplementary Information is available in the online version of the paper.

Acknowledgements This work was funded in part by the German Federal Ministry of Education and Research (BMBF), “Fluoropor” (grant number 03X5527) and “Molecular Interaction Engineering: From Nature’s Toolbox to Hybrid Technical Systems” (grant number 031A095C). We thank S. Wagner for helping with the photographs and R. Thelen for atomic force microscope measurements. We thank the Institute of Applied Materials (IAM-WPT) for helping with the Supplementary Video. This work was partly carried out with the support of the Karlsruhe Nano Micro Facility (www.kit.edu/knmf), a Helmholtz Research Infrastructure at KIT. We thank BASF and Evonik for providing chemicals.

Author Contributions F.K. and B.E.R. conceived the idea. F.K. designed the experiments, synthesized the material and performed the stereolithography processes. K.A. performed the microlithography process. W.B. performed X-ray diffraction and thermal gravimetric analysis measurements. C.R. performed white-light interferometry measurements. N.K., T.M.N. and K.S. performed scanning electron microscopy measurements. D.H. performed ultraviolet–visible measurements. F.K. wrote the manuscript and all authors contributed to the writing of the manuscript.

Author Information Reprints and permissions information is available at www.nature.com/reprints. The authors declare no competing financial interests. Readers are welcome to comment on the online version of the paper. Publisher’s note: Springer Nature remains neutral with regard to jurisdictional claims in published maps and institutional affiliations. Correspondence and requests for materials should be addressed to B.E.R. (Bastian.Rapp@kit.edu).

Reviewer Information Nature thanks J. Smay and the other anonymous reviewer(s) for their contribution to the peer review of this work.

METHODS

Materials. Amorphous silica nanopowder of type Aerosil OX50 was kindly provided by Evonik, Germany. Tinuvin 384-2 was kindly provided by BASF, Germany. Tetraethylenglycoldiacrylate (TEGDA), Sudan Orange G, diphenyl(2,4,6-trimethylbenzoyl)phosphine oxide, phenylbis(2,4,6-trimethylbenzoyl)phosphine oxide, gold(III) chloride, (3-methacryloxypropyl)dimethylchlorosilane and trimethylolpropane ethoxylate triacrylate were purchased from Sigma Aldrich, Germany. Ethanol, methanol, phenoxyethanol (POE) and hydroquinone were purchased from Merck, Germany. Hydroxyethylmethacrylate (HEMA), vanadium(III) chloride and chromium(III) nitrate were purchased from Alfa Aesar, Germany. All chemicals for the chemical resistance test were purchased from Merck, Germany.

Preparation of the nanocomposite. The individual components of the monomeric matrix were mixed before the dispersion process. Then the amorphous silica nanopowder was added in small increments to the mixture using a laboratory dissolver stirrer of type R 130 (purchased from IKA, Germany). The photoinitiator, inhibitor and absorber were added following a further homogenization step. The slurry was degassed using an ultrasonic bath or vacuum.

For benchtop stereolithography 37.5 vol% of Aerosil OX50 was dispersed in a monomer mixture of 60 vol% HEMA, 10 vol% TEGDA and 30 vol% POE. The mixture was blended with 0.2 wt% of diphenyl(2,4,6-trimethylbenzoyl)phosphineoxide, 0.1 wt% of hydroquinone and 0.05 wt% of Sudan Orange G (with respect to the amount of reactive monomer). For microstereolithography, microlithography and greyscale lithography 35 vol% of Aerosil OX50 was dispersed in a monomer mixture of 65 vol% HEMA, 35 vol% trimethylolpropane ethoxylate triacrylate. The mixture was blended with 0.5 wt% of phenylbis(2,4,6-trimethylbenzoyl)phosphineoxide, 0.5 wt% of hydroquinone and 0.45 wt% of Tinuvin 384-2 (referred to the amount of reactive monomer). Microfluidic chips were structured on top of a cured nanocomposite sheet. The micro-optical structures were structured on top of commercial fused silica slides. The slides were cleaned in acidic methanol for 45 min. The surface was then functionalized in a 100 mM solution of (3-methacryloxypropyl)dimethylchlorosilane in toluene before adding the slurry.

Stereolithography and direct structuring. For stereolithography, the nanocomposite was processed in a commercial stereolithography printer of type Asiga Pico 2 (purchased from 3DXS, Germany). Overcuring along the z-axis could be prevented by using the absorber Sudan Orange G. For micro(stereo-) lithography we used a custom-built microlithography system based on a digital mirror device, which we have previously described¹⁸. The system was complemented by a z-axis. Stereolithography parts were developed in a 1:1:1 vol/vol/vol solution of ethanol, water and POE. Micro(stereo-)lithography parts were developed in a 1:1 vol/vol solution of methanol and water.

Glass doping with metal salts. 0.1 wt% of gold(III) chloride, 0.5 wt% of vanadium(III) chloride and 0.5 wt% of chromium(III) nitrate were dissolved in ethanol, respectively. The brown parts, fabricated from a mixture with a solid loading of 40 vol%, were subsequently immersed in the solutions for 1 h. The brown parts were then dried at 50 °C for 1 h before the sintering process.

Heat treatment. Thermal debinding was performed in an ashing furnace of type AAF (purchased from Carbolite/Gero, Germany). Decomposition of the polymerized nanocomposites was characterized using thermal gravimetric analysis of type STA449F3 (instrument purchased from Netzsch, Germany). Sintering was performed in a high-temperature tube furnace of type STF16/450 (purchased from Carbolite/Gero, Germany). The parts were sintered at 1,300 °C at a pressure of 5×10^{-2} mbar with a heating rate of 3 K min⁻¹. A holding phase at 800 °C was set to evaporate molecular water and surface-bound silanol groups.

For sintering of the coloured glasses the furnace was flooded with nitrogen before the evacuation step.

Chemical resistance tests. Chemical stability of the sintered fused silica was assessed using a microfluidic chip which was probed with the following chemicals: 2-propanol, acetone, tetrahydrofuran, dichloromethane, chloroform, cyclohexane, n-hexane, toluene, aqueous sodium hydroxide solution, ammonia solution and hydrochloric acid.

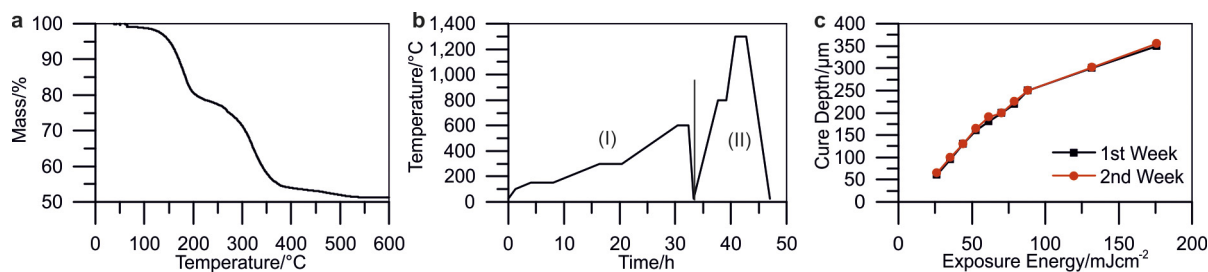
Glass characterization. The X-ray powder diffraction system of type D5000 (purchased from Siemens/Bruker, Germany) was used to ensure that no devitrification occurred during the sintering process. A dilatometer of type DIL402C (purchased from Netzsch, Germany) was used to characterize the thermal expansion of the sintered glass parts. A Raman microscope of type SENETERRA (purchased from Bruker, Germany) equipped with 532 nm and 785 nm lasers (depolarized) was used to perform Raman spectroscopy. Spectra recorded at 532 nm showed less fluorescence background and were selected for comparison of the samples. Spectra have been normalized to the maximum value. An X-ray photoelectron spectroscopy system of type PHI 5000 Versa Probe II (purchased from ULVAC-PHI Inc.) was used to show that the printed glass consists of pure fused silica glass. It was equipped with a scanning microprobe X-ray source (monochromatic Al K α (wavelength 1,486.6 eV) X-rays) in combination with an electron flood gun and a floating ion gun generating low-energy electrons (1.1 eV) and low-energy argon ions (6 eV) for charge compensation at isolating samples (dual beam technique), respectively. The angle between the sample surface and the analyser was set to 45°. Survey scans were recorded with an X-ray source power of 33 W and pass energy of 187.85 eV. Narrow scans of the elemental lines were recorded at 23.5 eV pass energy, which yields an energy resolution of 0.69 eV full-width at half-maximum (FWHM) at the Ag 3d_{5/2} elemental line of pure silver. Calibration of the binding energy scale of the spectrometer was performed using well established binding energies of elemental lines of pure metals (monochromatic Al K α : Cu 2p_{3/2} at 932.62 eV, Au 4f_{7/2} at 83.96 eV)²². All spectra were charge-referenced²³ to Si 2p (VYCOR, vitreous silica) at 103.5 eV.

Surface characterization. Surface roughness was measured using an atomic force microscope of type Dimension Icon (purchased from Bruker, USA). Shrinkage during sintering was measured using a white light interferometer of type Contour GT-K (purchased from Bruker, USA).

Optical characterization. Optical transmission was characterized using an ultraviolet–visible spectrometer of type Evolution 201 (purchased from Thermo Scientific, Germany) and a Fourier transform infrared spectrometer of type Frontier (purchased from Perkin Elmer, Germany). The transmission spectrum was recorded on vacuum sintered glass slides with a thickness of 1 mm. Quartz glass slides with a thickness of 1 mm (purchased from Plano, Germany) were used as reference samples. Transmission of nanocomposites was measured using fused silica cuvettes of type QS with a path length of 10 mm (purchased from Hellma Analytics, Germany).

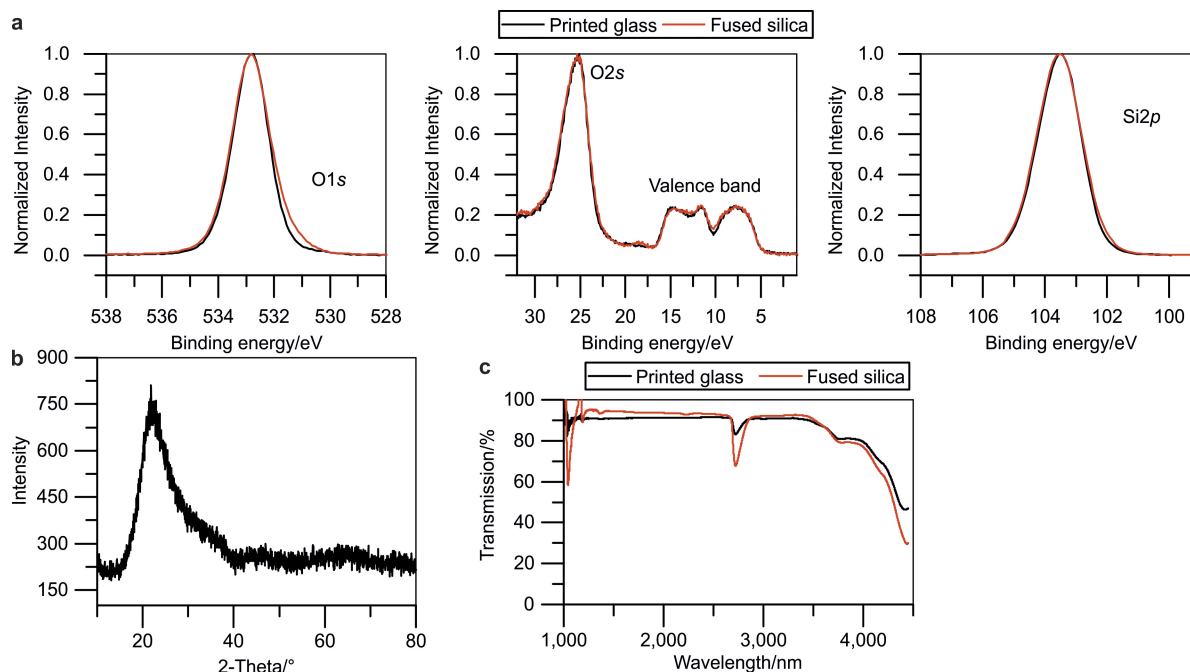
Data availability. The authors declare that the data supporting the findings of this study are available within the paper and its Supplementary Information files. Source data for figures are provided in the HTML version of the paper.

22. Seah, M., Gilmore, I. & Beamson, G. XPS: binding energy calibration of electron spectrometers 5—re-evaluation of the reference energies. *Surf. Interf. Anal.* **26**, 642–649 (1998).
23. Moulder, J. F., Stickle, W. F., Sobol, P. E & Bomben, K. D. *Handbook of X-ray Photoelectron Spectroscopy: a Reference Book of Standard Spectra for Identification and Interpretation of XPS Data* 238 (Physical Electronics Eden Prairie, 1995).



Extended Data Figure 1 | Characterization of the nanocomposite processing. **a**, Thermal gravimetric analysis of the cured nanocomposite used for stereolithography. The sample had a solid loading of 37.5 vol% SiO₂. **b**, Corresponding heating programme for thermal debinding (I) and sintering (II) used for the composite shaped using stereolithography.

c, Stereolithography cure depth (depth of a voxel upon exposure, corresponding to the penetration of the polymerization front during exposure) versus the laser power. The nanocomposites are highly stable and can be used for weeks with the same polymerization parameters.



Extended Data Figure 2 | Material and surface characterization of sintered glass. **a**, X-ray photoelectron spectroscopy narrow scans of elemental lines of printed and sintered glass compared to commercial fused silica glass. All spectra show virtually no difference between sintered fused silica glass and commercial fused silica glass. **b**, X-ray

diffraction measurement shows that no devitrification occurs during the sintering process. Devitrification would present in the form of narrow peaks and spikes in the spectrum. **c**, Fourier transform infrared (FTIR) measurements of sintered glass compared to commercial fused silica glass.